A simple diagnostic for eyewall replacement based on Pressure-Wind relationship

Ping Lu[1], Long Yang[2], Jishi Zhang[1], Danyang Wang[1], Dingchi Zhao[1], Xing Huang[1], Xiaomeng Huang[1], Yanluan Lin [1]

[1]Department of Earth System Science, Tsinghua University, Beijing, China
[2]School of Geography and Ocean Science, Nanjing University, Nanjing, China

Corresponding authors:
Ping Lu, luping@mail.tsinghua.edu.cn
Yanluan Lin, yanluan@mail.tsinghua.edu.cn

Key Points:

- We present a simple diagnostic based on storm intensity, size and latitude as a diagnostic for eyewall replacements.
- It reproduces the intensification and weakening phases of eyewall replacements, and coincides with 70% of observed concentric eyewalls.
- The diagnostic may be expressed as a latitude-irrelevant Rossby Number, related to the peakedness of wind.

Abstract

Eyewall replacements occur in 70% of major tropical cyclones (TCs), and are associated with rapid changes in storm intensity and rapid broadening of strong winds. In this study, we present to use the radial gradient of absolute angular momentum with Holland's wind profile as a simple diagnostic for eyewall replacement as internal variability of the storm. The diagnostic is solely dependent on the maximum wind speed, the radius of maximum wind, and the latitude and found to coincident with 70% of satellite observed concentric eyewalls for 1991-2020. The diagnostic can be expressed as a latitude-irrelevant Rossby Number of primary eyewall, varying with the peakedness of wind. It highlights the importance of pressure-wind relationship in eyewall replacement and provides a valuable tool to improve the understanding, modeling and risk assessment of storms with eyewall replacements.

Plain Language Summary

Eyewall replacements are complicated processes associated with rapid changes in storm structure and intensity as results of storm internal variability and interaction with the environment. In this study, we find a simple diagnostic, based on three basic storm characteristics, may explain 70% of satellite observed concentric eyewalls from 1991-2020.

1. Introduction

Tropical cyclones (TCs), are commonly characterized by a tranquil low pressure center, i.e. storm eye, and a ring of intense convection called the eyewall (the term is a direct representation of the ~16 km's tall cloud wall that one can visually see from the storm eye). An eye and one ring of eyewall constitute the typical structure of TC. Observations have long shown, however, that for some TCs there exists a concentric (secondary or even tertiary) eyewall (CE) outside the primary eyewall (Black & Willoughby, 1992; Willoughby et al., 1982), with the moat region between them, a nearly echo-free annulus on radar, taking on the characteristics of the eye (Houze et al., 2007). The occurrence of CE is usually accompanied by the weakening of primary eyewall, which eventually dissipates while the outer eyewall contracts and takes over, in a process called eyewall replacement cycle (ERC). ERCs can last a few hours to more than a day (vary significantly among storms), during which storms undergo large oscillations in intensity and size, and is regarded as a 'key process in hurricane intensity change' (Houze et al., 2007). Storms with ERCs can have serious impacts to coastal communities, especially the rapid changes in intensification (e.g., Hurricane Andrew 1992, Hurricane Irma 2017) and rapid broadening of strong winds (e.g., Hurricane Katrina 2005) just prior to landfall.

CEs may not be captured by visible or infrared images because of the shielding from cirrus canopy and outward-slanting primary eyewall. It was not until 2004, when long-term passive microwave data was analyzed, that we learned the percentage of CEs is 'far higher than previously thought'(Hawkins et al., 2006; Hawkins & Helveston, 2004). About 70% of major hurricanes (Saffir-Simpson Hurricane Scale, SSHS category 3-5, wind speed > 47 m s^{-1}) show CEs (Hawkins et al., 2006; Hawkins & Helveston, 2004; Kossin & Sitkowski, 2009a; Hung-Chi Kuo et al., 2009). Compared with single-eyewall storms, CE storms are found to be associated with stronger wind speed, smaller eye diameter, colder infrared brightness temperatures, higher sea surface temperatures, weaker environmental wind shear, and lower latitudes (Hence & Houze, 2012; Kossin & Sitkowski, 2009a; Yang et al., 2013). Unlike single-eyewall storms, the weakening of intensity of CE storms typically occurs in an environment that is not indicative of weakening (Kossin & DeMaria, 2016) and is accompanied with maintaining or increasing convective activity (Yang et al., 2013).

Mechanisms of CE formation have been investigated from various perspectives, from the ambient environment (e.g. humidity (Ge, 2015; Hill & Lackmann, 2009), beta shear(Fang & Zhang, 2012), storm interaction with midlatitude jet (Dai et al., 2017), upper-level trough (Molinari & Vollaro, 1990; Nong & Emanuel, 2003), nearby vortices(H-C. Kuo et al., 2004; Hung-Chi Kuo et al., 2008)), to the internal dynamics of the storm (e.g. vortex Rossby waves-mean flow interaction (Montgomery & Kallenbach, 1997; Terwey & Montgomery, 2008), potential vorticity in rainbands (Judt & Chen, 2010; May & Holland, 1999), supergradient wind and unbalanced boundary layer response (Abarca & Montgomery, 2013, 2014; Bell et al., 2012; Huang et al., 2012), positive feedback among radial vorticity gradient, frictional convergence and moist convection (Kepert, 2013), wind-induced surface heat exchange(Cheng & Wu, 2018; Nong & Emanuel, 2003), outer-core latent heating (Bell et al., 2012; Rozoff et al., 2012; Wang, 2009), timescale of filamentation vs. convection (Rozoff et al., 2006) , ice-phase microphysics (Zhou & Wang, 2011)).

In this study, we present a simple diagnostic, the lower bound of radial gradient of absolute angular momentum computed with Holland's 2010 (hereafter H10) reaching a critical threshold, $\frac{\partial M}{\partial r}_{min} \rightarrow 0$, as a diagnostic for eyewall replacement. The diagnostic takes input of three basic storm characteristics, maximum wind speed (V_m), radius of maximum wind (R_m), and latitude of the storm. With observed V_m, R_m and latitude from International Best Track Archive for Climate Stewardship (IBTrACS, Knapp et al. 2018), the diagnostic is shown to coincide with ~70% of satellite-observed CEs during 1991-2020. We are surprised that the information of a storm undergoing ERC, previously recognized only by satellite observations or flight-level aircraft observations, may be folded in just three numbers.

The diagnostic is introduced in Section 2. Section 3 describes satellite observations of CEs for global storms 1991-2020, which are used to evaluate the diagnostic in Section 4. The peakedness of wind is discussed in Section 5. Section 6 summarizes the paper with suggestions on future directions.

2. Mathematical expression of the diagnostic

In the frictional inflow layer of a circular vortex, the principal balance is between radial advection of angular momentum and frictional torque acting on the azimuthal velocity (Lu et al., 2018; Ooyama, 1969),

$$u\frac{\partial M}{\partial r} \cong -r\frac{\partial \tau_\theta}{\partial z}\,, \qquad (1)$$

where u is the radial velocity, r is the radius from the storm center, M is the absolute angular momentum per unit mass ($M = rV + 0.5fr^2$, where V is the azimuthal wind speed and f is the Coriolis parameter), and τ_θ is the azimuthal turbulent stress.

Eqn.(1) is used in the simple physics-based TC rainfall model, TCR, for risk assessment purpose (Emanuel, 2017; Feldmann et al., 2019; Gori et al., 2022; Lu et al., 2018; Xi et al., 2020; L. Zhu et al., 2013, 2021). Together with continuity equation, Eqn.(1) gives estimates of vertical velocity from frictional convergence at the top of boundary layer. Previous case study analysis (Lu et al., 2018) showed that rainfall from frictional convergence contribute to over 70% of total rainfall in TCR, and Holland's wind model, when applied in TCR, would result in rainfall estimates most close to downscaled modeling, better than theoretical parametric wind models of Emanuel 2004 (hereafter E04), Emanuel and Rotunno 2011 (hereafter ER11) and Chavas et al. 2015 (hereafter C15).

Fig.1a shows V from a widely used parametric wind model, Holland's 2010 (H10) and the sign of u from Eqn. (1). For ordinary TCs (blue line), with a predefined V from H10 with observed V_m and R_m , $\partial M/\partial r$ remains positive along r, resulting in negative u from Eqn. (1), indicating consistent convergence from large radius to eyewall. As to the most intense and compact TCs (red dashed line), a predefined V from H10 could make the lower bound of $\partial M/\partial r$, $\frac{\partial M}{\partial r}_{min}$, gets to zero (or even negative) at some point along r (which will never happen in real TCs due to divergence of the flow), resulting in the unrealistic u from Eqn. (1) ($u \rightarrow \infty$ or $u > 0$) and a crude picture of secondary eyewall occurrence. Such singularity would not occur with theoretical wind models E04, ER11 and C15, for the thermodynamic solutions ensure $\partial M/\partial r$ always positive. But with semi-empirical wind model like Holland 1980 (hereafter H80) and H10, where V is deduced from an empirical pressure distribution (Eqn. 2, calculating pressure p from storm central pressure p_c using an empirical b parameter controlling the peakedness of wind) and cyclostrophic balance (Eqn. 3),

$$p = p_c + \Delta p_c \, e^{-\left(\frac{r}{R_m}\right)^b}, \qquad (2)$$

$$V = V_m \left\{ \left(\frac{r}{R_m}\right)^{-b} e^{\left[1-\left(\frac{r}{R_m}\right)^{-b}\right]} \right\}^{\frac{1}{2}}, \qquad (3)$$

$\frac{\partial M}{\partial r}_{min} \rightarrow 0$ may occur for storms featuring large V_m and small R_m. In this study we use H10 (Eqn. 4), which improves upon Eqn. (3) by allowing b to vary with storms and exponent x to adjust to observations (Detailed in Text S1).

$$V = V_m \left\{ \left(\frac{r}{R_m}\right)^{-b_s} e^{\left[1-\left(\frac{r}{R_m}\right)^{-b_s}\right]} \right\}^{x}, \qquad (4)$$

We start with a simple set of parameter b_s = 1.8 from a baseline hurricane discussed in H10 with sensitivity analysis in Section 5.

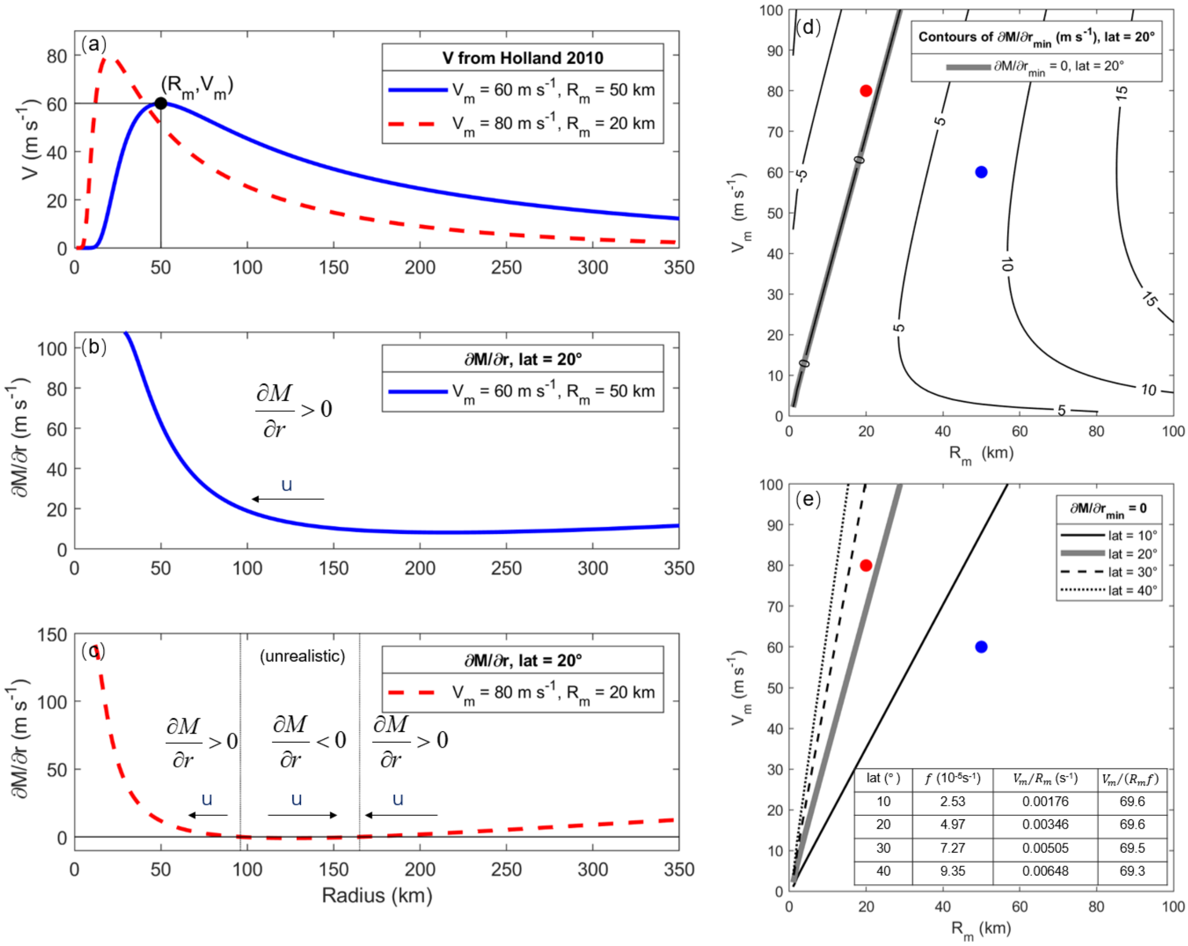

lat (°)	f (10^{-5}s^{-1})	V_m/R_m (s^{-1})	$V_m/(R_m f)$
10	2.53	0.00176	69.6
20	4.97	0.00346	69.6
30	7.27	0.00505	69.5
40	9.35	0.00648	69.3

Fig.1.(a) V and (b,c) $\partial M/\partial r$ along r for two idealized vortices. The parametric wind model used is H10. Parameter $b_s = 1.8$ from a baseline hurricane is used (detailed in Section 5). (d) Contours of the lower bound of $\partial M/\partial r$ along radius for varying V_m and R_m. (e) Contours of $\partial M/\partial r = 0$ for varying latitudes. Table in (e) shows values of Rossby Number on $\partial M/\partial r = 0$ with varying latitudes.

Fig.1d shows contours of the $\frac{\partial M}{\partial r}_{min}$ with varying V_m and R_m. We name the triangle region with $\frac{\partial M}{\partial r}_{min} < 0$ the 'singular zone', namely V_m and R_m falling in 'singular zone' induces singularity in Eqn.(1). The 'singular zone' features large V_m and small R_m, consistent with our previous knowledge that eyewall replacements occur for the most intense and compact storms. $\frac{\partial M}{\partial r}_{min} = 0$ for H10 results in a straight line through (0,0) on the V_m - R_m plane (this is a unique property of H10 and not found for other wind models, Fig.S1), intuitively showing that, with H10, the high relative vorticity near the eyewall cannot continue to increase with disrupted inward advection of angular momentum ($\frac{\partial M}{\partial r}_{min} \to 0$, singularity of Eqn 1). Furthermore, the slope of $\frac{\partial M}{\partial r}_{min} = 0$ is found scaled by f, i.e. the Rossby Number stays constant with varying latitudes on $\frac{\partial M}{\partial r}_{min} = 0$ (Fig.1e, Fig.4c), showing the relative vorticity a storm can achieve is dependent on planetary vorticity. In other words, a storm needs to be more intense and compact to trigger CE at higher latitudes, consistent with observations that CE storms generally have lower latitudes compared to non-CE storms (Kossin & Sitkowski, 2009b).

3. Data

One common practice in systematically detecting CEs is analyzing the 85 GHz passive microwave data. If two rings of intense convection separated by a nearly echo-free annulus is observed, the storm is labeled as showing CE (criteria vary slightly among studies, e.g., outer ring covers at least 2/3 of a circle (Hung-Chi Kuo et al., 2009), or 3/4 of a circle (Kossin & Sitkowski, 2009a)). In this study, the CEs were detected by analyzing 85/92 GHz brightness temperature T_b from Special Sensor Microwave/Imager (SSM/I), Special Sensor Microwave Imager and Sounder (SSMIS) and the Tropical Rainfall Measuring Mission Microwave Imager (TMI) from 1991 to 2020. 22837 snapshots of 2462 storms were collected, covering 77.7% of the total 3169 storms documented in IBTrACS from 1991-2020. Time intervals between successive snapshots of one storm vary greatly, with a mean of 16.4 h and standard deviation of 18.2 h.

We adopt the criteria of CE in Kuo et al. 2009, i.e., $T_b \leq 230\ K$ covering at least 2/3 of a circle, and identify 610 snapshots of 311 storms as showing CE (hereafter CE group), with the rest of storms non-CE group. Snapshot locations and tracks of the CE group are shown in Fig.2a. The diagnostic $\frac{\partial M}{\partial r}_{min}$ is dependent on three parameters: V_m, R_m, and f (computed from latitude of the storm center). We obtain observations of these three parameters from IBTrACS version 4.0 (Knapp et al. 2018). Note that while V_m and f are available for most storms during their lifetime, R_m is only available for 216 CE storms and 1317 non-CE storms during part of the storm lifetime. Only storms with V_m, R_m and f observations are used in the following analysis.

4. Results

Sitkowski et al. (2011) expanded the paradigm first established by Willoughby et al. (1982) and documented the three phases of ERC: 1) *Intensification*, characterized by outer wind maximum undergoing contraction and inner wind maximum reaching peak intensity (often associated with rapid intensification); 2) *Weakening*, inner wind maximum weakens and as the outer wind maximum contracts and surpasses inner wind maximum, at the same time, concentric rings appear on microwave imagery near the midpoint of this phase; 3) *Reintensification*, inner wind maximum decays and outer wind maximum takes over as primary eyewall.

According to Sitkowski et al. (2011), all CE snapshots are observed in *Weakening* phase, during which V_m and R_m documented in IBTrACS may or may not be of the inner eyewall. Note that the diagnostic $\frac{\partial M}{\partial r}_{min}$ should take input of the inner eyewall. To avoid such complexities, we first focus on the lifetime minimum $\frac{\partial M}{\partial r}_{min}$ of each storm (targeting at the *Intensification* phase prior to the observed CEs), and then look into the timing of CE snapshots following the lifetime minimum $\frac{\partial M}{\partial r}_{min}$.

4.1 Lifetime minimum $\frac{\partial M}{\partial r}_{min}$

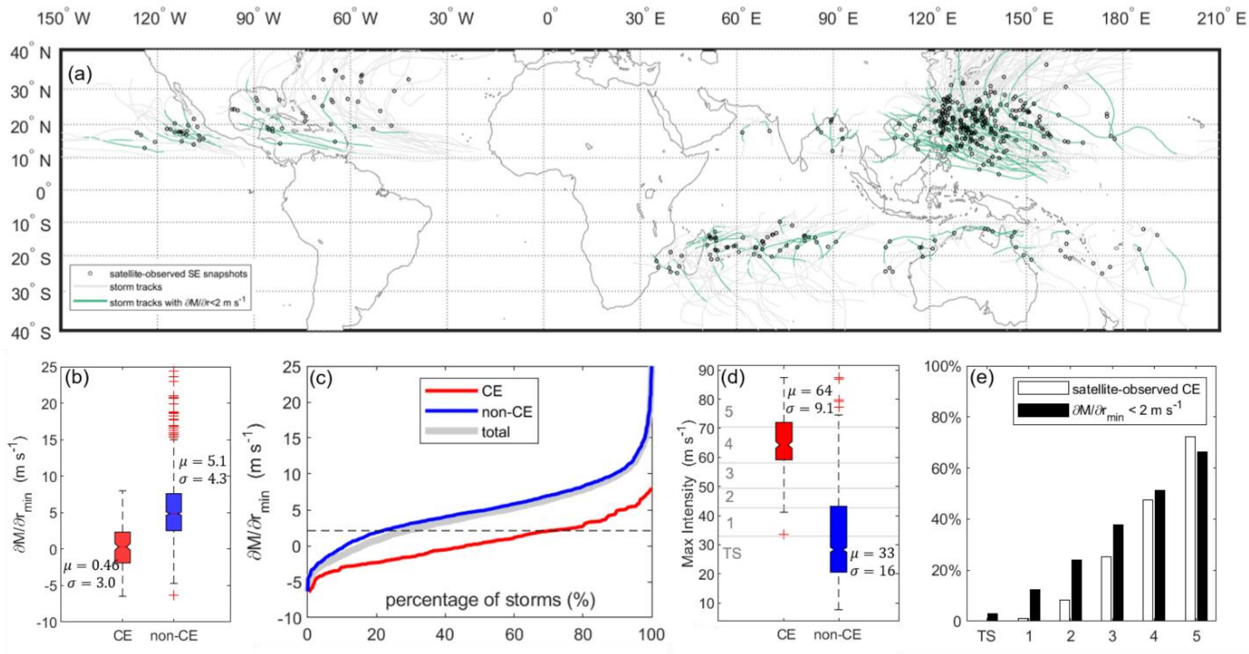

Fig.2. (a) Locations of the CE snapshots and tracks of the CE storms. Green line marks the time window associated with $\frac{\partial M}{\partial r}_{min} < 2\ m\ s^{-1}$ and the subsequent 24 h. (b) Lifetime minimum $\frac{\partial M}{\partial r}_{min}$ values of CE vs non-CE. (c) same as (b) shown in c.d.f. (d) Lifetime maximum windspeed of CE vs non-CE, with SSHS categories labeled. (e) Percentage of occurrence among SSHS categories of satellite observations and $\frac{\partial M}{\partial r}_{min} < 2\ m\ s^{-1}$.

Lifetime minimum $\frac{\partial M}{\partial r}_{min}$ shows significant difference between CE vs non-CE groups (Fig.2b), with p value for the F-test being 1.14×10^{-10}. The mean of $\frac{\partial M}{\partial r}_{min}$ is 0.46 (very close to 0) and 5.1 with a standard deviation 3.0 and 4.3 for the CE and non-CE group, respectively. With c.d.f. of $\frac{\partial M}{\partial r}_{min}$ (Fig.2c), as well as Probability of Detection and False Alarm Ratio (Table S1), we choose to use a threshold of $2\ m\ s^{-1}$, which separates about 75%~80% of storms in CE vs non-CE groups, as a benchmark threshold for $\frac{\partial M}{\partial r}_{min} \rightarrow 0$ for the rest of analysis. The 20% of non-CE storms with $\frac{\partial M}{\partial r}_{min} < 2\ m\ s^{-1}$ are likely associated with ERC but not captured by microwave observations (detailed in Table S1), and the 30% of CE storms with $\frac{\partial M}{\partial r}_{min} > 2\ m\ s^{-1}$ are likely associated with storm interaction with the environment (discussed in Section 4.2). The spread of observed CE among storm categories is generally reproduced by $\frac{\partial M}{\partial r}_{min} < 2\ m\ s^{-1}$ (Fig.2e), indicating the ability of the diagnostic to work among various storm categories.

4.2. Timing

For storms associated with lifetime minimum $\frac{\partial M}{\partial r}_{min} < 2\ m\ s^{-1}$ (70% of the CE group, 268 CEs), we plot the composite evolution of $\frac{\partial M}{\partial r}_{min}$ aligned at the time when $\frac{\partial M}{\partial r}_{min}$ first gets below $2\ m\ s^{-1}$ (blue line and shading in Fig.3a). There is a sharp drop of $\frac{\partial M}{\partial r}_{min}$ below the threshold followed by a gradual increase, accompanied by a surge of observed CEs (Fig.3c). The surge of observed CEs gradually decays in 4-5 days, in a very similar distribution as the time window associated with $\frac{\partial M}{\partial r}_{min} < 2\ m\ s^{-1}$ (Fig.3d). In fact, 77% of CEs occur within 2 days after the diagnostic reaches below 2 m s^{-1}, and 89% within 4 days (Table 1). This temporal coincidence indicates that the diagnostic may have captured the timing of onset and subsequent duration of ERCs.

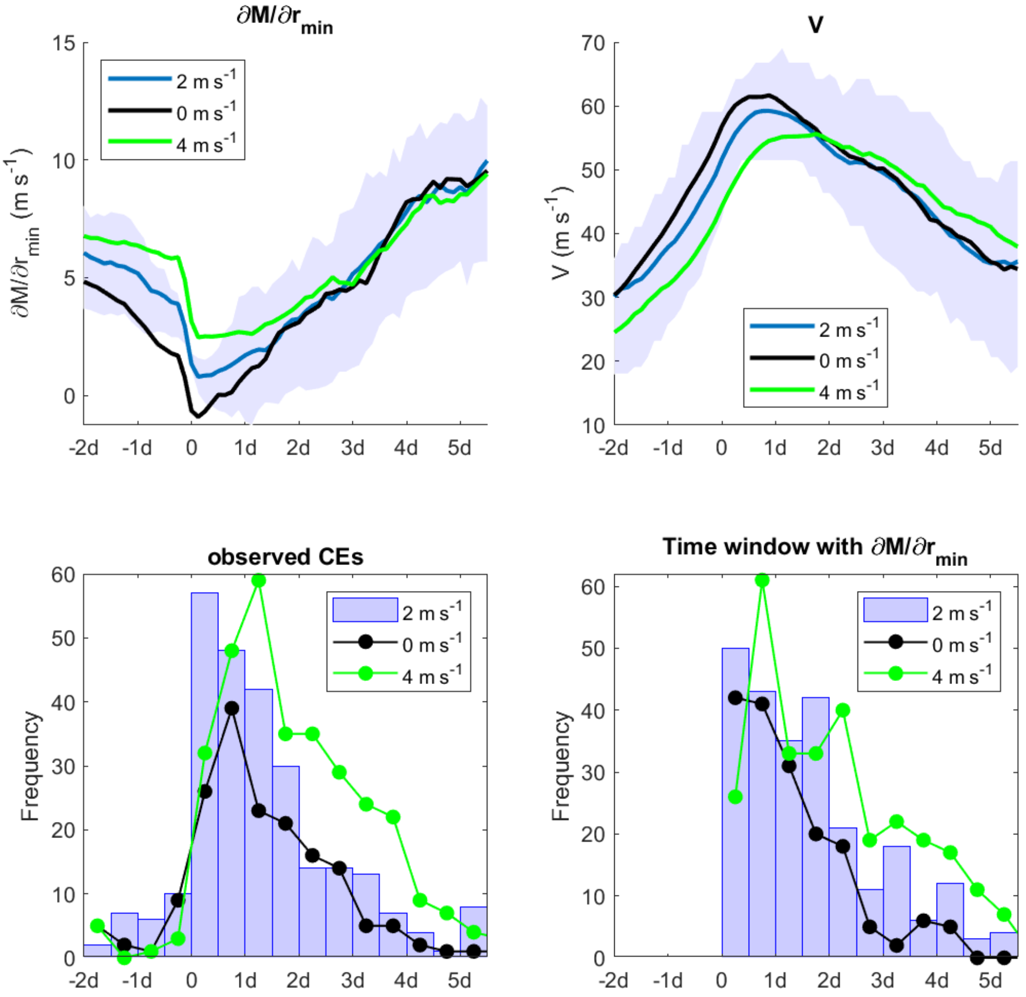

Fig.3.(a) Evolution of $\frac{\partial M}{\partial r}_{min}$ for storms in CE group aligned at the time when $\frac{\partial M}{\partial r}_{min}$ <2 m s^{-1}, 0 m s^{-1}, 4 m s^{-1}, shading indicates the 25th and 75th percentile of spread with 2 m s^{-1}; (b) same as (a) but for the evolution of V_m; (c) incidence of CE snapshots regarding to the time when $\frac{\partial M}{\partial r}_{min}$ < 2 m s^{-1}, 0 m s^{-1}, 4 m s^{-1}; (d) distribution of the time window associated with $\frac{\partial M}{\partial r}_{min}$ < 2 m s^{-1}, 0 m s^{-1}, 4 m s^{-1}. The number of CEs in the composites is 268, 172, 333 for lifetime minimum $\frac{\partial M}{\partial r}_{min}$ <2 m s^{-1}, 0 m s^{-1}, 4 m s^{-1}, respectively (details in Table S2).

The composite evolution of V_m shows rapid increases as $\frac{\partial M}{\partial r}_{min}$ approaches $2\ m\ s^{-1}$ (30.0 knots of increase in composite mean of V_m from -18 h to 6 h), followed by a gradual increase to peak intensity in 24 h (blue line and shading in Fig.3b). Together with the surge of CEs following $\frac{\partial M}{\partial r}_{min} < 2\ m\ s^{-1}$, this constitutes a clear picture of the *Intensification phase* (often characterized by rapid intensification) and *Weakening phase* (characterized by weakening and appearance of CEs on microwave imagery) of ERCs documented by Sitkowski et al. (2011). This is also consistent with previous observational studies that CEs on average are observed around the time of lifetime maximum intensity *(Hung-Chi Kuo et al., 2009; Yang et al., 2013)*. From this perspective, $\frac{\partial M}{\partial r}_{min} < 2\ m\ s^{-1}$ may an indicator of the transition between the *Intensification phase* and *Weakening phase* of ERCs. The above findings do not vary much if we change the threshold from 2 m s^{-1} to 0 m s^{-1} or 4 m s^{-1} (Fig.3 and Table S1). With a stricter threshold, the number of CEs used in the composite is smaller, associated with more rapid intensification and higher intensity.

Some observed CEs are associated with relatively large values of $\frac{\partial \mathrm{M}}{\partial \mathrm{r}}_{\mathrm{min}}$, and are not captured by this diagnostic. One notable example is the last observed CE of Super Typhoon Muifa (2011, Fig.S2). Seven CEs were observed during Muifa, while six are associated with ERCs start with $\frac{\partial \mathrm{M}}{\partial \mathrm{r}}_{\mathrm{min}}$ < 2 m s^{-1}. The last CE of Muifa, separated by non-CEs from previous ERCs, is associated with $\frac{\partial \mathrm{M}}{\partial \mathrm{r}}_{\mathrm{min}}$ > 7 m s^{-1} for over 24 hours. As discussed in more detail in Zhu and Yu (2019), the last observed CE of Muifa characterized strong interactions with the environment while earlier CE of Muifa occurred in a relatively quiet environment. It's a clear sign that there exist multiple mechanisms for CE occurrence, and some do not directly involve V_m, R_m, f, such as the interaction of the vortex with mid-latitude jet (Dai et al., 2017) or upper-level trough (Molinari & Vollaro, 1990; Nong & Emanuel, 2003). Generally, CEs not captured by this diagnostic has higher latitudinal distributions (Fig.S3). The attribution of different CE mechanisms is a very interesting topic for future studies.

5. Discussion on the peakedness of wind

The peakedness of wind in H10 is controlled by the b_s parameter (how fast pressure deficit drop along the radius). Higher value of b_s results in higher peakedness of wind, more expanded 'singular zone' on $V_m - R_m$ plane, lower values of $\frac{\partial \mathrm{M}}{\partial \mathrm{r}}_{\mathrm{min}}$ and higher chances of ERCs. In Section 4, we use $b_s = 1.8$, which comes from a baseline hurricane discussed in

H10. The baseline hurricane is composed of sea surface temperature $SST = 28\,°C$, latitude $\varphi = 20°$, $\Delta p_c = 55\ hPa$, intensity change $\partial p_{cs}/\partial t = 3\ hPa\ s^{-1}$,translational speed $v_t = 5\ m\ s^{-1}$. These result in values of $b_s = 1.8$, $x_n = 0.8$ and $r_n/R_m = 15$. H10 provides a statistical approach to better estimate $\boldsymbol{b_s}$ from p_c, φ and v_t,

$$\boldsymbol{b_s = -4.4 \times 10^{-5}\Delta p_c{}^2 + 0.01\Delta p_s + 0.03\frac{\partial p_c}{\partial t} - 0.014\varphi + 0.15 v_t{}^{0.6\left(1-\frac{\Delta p_c}{215}\right)} + 1.0}, \quad (5)$$

here we show the sensitivity of the diagnostic to b_s using Eqn (5).

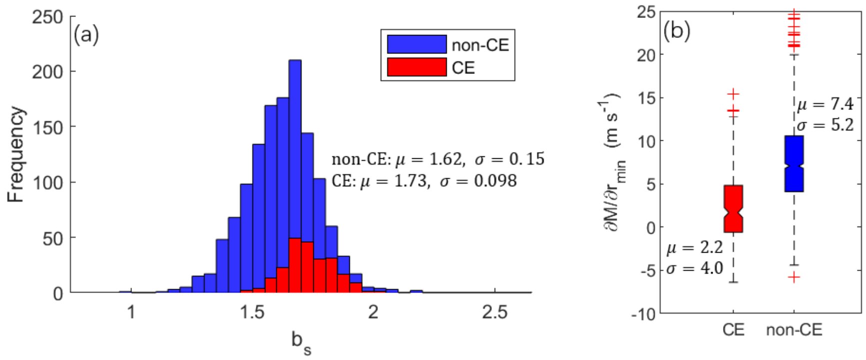

(c)	$V_m/(R_m f)$ on $\frac{\partial M}{\partial r}_{min} = 0$ with varying b_s and latitudes					
lat (°)	$b_s = 1.4$	$b_s = 1.5$	$b_s = 1.6$	$b_s = 1.7$	$b_s = 1.8$	$b_s = 1.9$
10	114.4	102.5	91.1	80.1	69.6	59.6
20	114.3	102.4	91.0	80.1	69.6	59.6
30	114.2	102.3	91.0	80.0	69.5	59.5
40	114.1	102.2	90.8	79.9	69.3	59.4

Fig.4. (a) Lifetime maximum b_s values computed for CE and non-CE using Eqn. (5) with inputs from IBTrACS. The mean and standard deviation of b_s for both groups are labeled. (b) Same as in Fig.2b but use b_s from Eqn.(5) instead of $b_s = 1.8$. (c) $V_m/(R_m f)$ on $\frac{\partial M}{\partial r}_{min} = 0$ with varying b_s and latitudes.

Generally CE storms are associated with higher b_s than non-CE storms (with a mean of 1.73 vs 1.62 for CE vs non-CE groups). The baseline value $b_s = 1.8$ is higher than most of the storms, therefore using the varying b_s from Eqn.(5) results in slightly higher $\frac{\partial M}{\partial r}_{min}$ for most storms, but still with significant difference between CE vs non-CE groups (Fig.4b). Taking a threshold of 4 m s^{-1}, the diagnostic with varying b_s shows very similar evolution and a surge of observed CEs (Fig.S4) as the diagnostic with fixed $b_s = 1.8$ and a threshold of 2 m s^{-1} (Fig.3).

It's worth noted that ERCs can have 'rapid and substantial effect on wind-pressure relationship' (Kossin, 2015), therefore Eqn.(5) may not give accurate values of b_s for CE storms. The desired b_s to be used in the diagnostic $\frac{\partial M}{\partial r}_{min}$ should depict the peakedness of the inner eyewall. Since H10 didn't distinguish observations from inner vs outer eyewalls for CE storms in deriving Eqn.(5), the b_s from Eqn.(5) may be biased towards low values for the use in the diagnostic $\frac{\partial M}{\partial r}_{min}$. Taking this into account, also in preference to a simple diagnostic, we propose to use a fixed value of $b_s = 1.8$ in computing $\frac{\partial M}{\partial r}_{min}$, as evaluated in Section 4.

6. Summary and Discussions

We propose a simple diagnostic, the lower bound of radial gradient of absolute angular momentum computed with H10 reaching a critical threshold, $\frac{\partial M}{\partial r}_{min} \to 0$, as a diagnostic for eyewall replacement. As approaching the critical threshold, boundary layer radial inflow is disrupted, limiting inward advection of angular momentum to the inner-core but favoring the spinup of an outer eyewall (and resulting drastic halt of storm intensification while the storm environments stay stable, as illustrated in our parallel work Lu et al. 2022). This diagnostic is a crude representation of internal variability of the storms and is shown to be associated with ~70% satellite-observed CEs. It highlights the importance of pressure-wind relationships and the role of secondary circulation in controlling the structure (and intensity, Lu et al. 2022) evolution of TCs.

The diagnostic is dependent on three storm characteristics, V_m, R_m and f. It depicts ERC as a storm entering the 'singular zone', featuring large V_m and small R_m, on the $V_m - R_m$ plane. It intuitively shows that, with H10, the high relative vorticity near the eyewall cannot continue to increase with disrupted inward advection of angular momentum ($\frac{\partial M}{\partial r}_{min} \to 0$, singularity of Eqn.(1)). This corresponds nicely with observations that CEs are associated with stronger wind speed and smaller eye diameter (Kossin & Sitkowski, 2009a; Hung-Chi Kuo et al., 2009; Yang et al., 2013). Environmental conditions (e.g. higher sea surface temperature, weaker environmental wind shear (Kossin & Sitkowski, 2009a; Yang et al., 2013), higher humidity(Hill & Lackmann, 2009)) and internal processes (e.g. the wind-induced surface heat exchange (Cheng & Wu, 2018; Nong & Emanuel, 2003), outer-core latent heating (Bell et al., 2012; Rozoff et al., 2012)) that favor the development of intense and compact storms will contribute to the development of ERC by pushing the storm into the 'singular zone'. But once inside the 'singular zone' and ERC starts (moat forms), the intensity of inner eyewall will no longer respond to favorable environment. This is consistent with the observations that the drop of V_m during ERC typically occurs in an environment that is not indicative of weakening (Kossin & DeMaria, 2016), and accompanied by steady or increasing convective activity (Yang et al., 2013). The ~30% of satellite-observed CEs not captured by this diagnostic generally have higher latitudinal distributions, and might be related to storm interaction with mid-latitude jet or upper-level trough.

Furthermore, the slope of the 'singular zone' is found to scaled by f. In other words, the diagnostic may be expressed as a latitude-irrelevant Rossby Number, related to the peakedness of wind. It intuitively shows that the relative vorticity a storm can achieve is dependent on planetary vorticity, and a storm needs to be more intense and compact to trigger CE at higher latitudes, which is consistent with observations that CE storms have lower latitudes compared to non-CE storms (Kossin & Sitkowski, 2009b). This is a unique and intriguing property of H10 and worth further investigation in the future.

Despite its great impact on storm size and intensity, ERC has rarely been accounted for in statistical intensity prediction or risk assessment of TCs. The simple form of this diagnostic makes it possible. We look forward to improvements in the modeling of TC intensity and TC-induced hazards, especially TC rainfall modeling, where the singularity was first observed.

Last but not least, the eyes of TCs have long been viewed as singularities of the atmospheric systems, although the explicit mathematical expression of such a singularity has not yet been revealed. If we shift our focus from intense convection of the storm, i.e., eyewalls, to the opposite of them, i.e., the eye and the moat, then ERC is not only the emergence of an outer eyewall gradually contracts and replaces inner eyewall, but also the emergence of a moat that gradually joins the eye. In this study, the occurrence of CE, or the occurrence of the moat, is found to take form of a singularity ($\partial M/\partial r \to 0$). Given that the moat is "dynamically similar to the eye" (Houze et al., 2007) and eventually becomes part of the eye, we are thrilled to think this diagnostic may shed light on an explicit form of singularity of the eye.

Acknowledgments.

We are truly grateful for the shared data from Prof. Hung-Chi Kuo, comments and encouragement from Prof. Kerry Emanuel, and detailed feedback and suggestions from Rohini Shivamoggi and constructive comments from two anonymous reviewers. This study is based upon work supported by the National Natural Science Foundation of China grant 42005116 (PL) and grant 42130603 (YL).

Open Research

IBTrACS dataset is openly available from NOAA NCEI at https://doi.org/10.25921/82ty-9e16 as cited in Knapp et al. (2018, 2010).

SSM/I dataset is openly available from NOAA NCEI at https://doi.org/10.7289/V5SJ1HKZ as cited in Wentz et al. (2013).

TMI dataset is openly available from NASA GES DISC at https://doi.org/10.5067/GPM/TMI/TRMM/1B/05 as cited in TMI (2017).

References

Abarca, S. F., & Montgomery, M. T. (2013). Essential Dynamics of Secondary Eyewall Formation. *Journal of the Atmospheric Sciences*, *70*(10), 3216–3230. https://doi.org/10.1175/JAS-D-12-0318.1

Abarca, S. F., & Montgomery, M. T. (2014). Departures from Axisymmetric Balance Dynamics during Secondary Eyewall Formation. *Journal of the Atmospheric Sciences*, *71*(10), 3723–3738. https://doi.org/10.1175/JAS-D-14-0018.1

Bell, M. M., Montgomery, M. T., & Lee, W.-C. (2012). An Axisymmetric View of Concentric Eyewall Evolution in Hurricane Rita (2005). *Journal of the Atmospheric Sciences*, *69*(8), 2414–2432. https://doi.org/10.1175/JAS-D-11-0167.1

Black, M. L., & Willoughby, H. E. (1992). The Concentric Eyewall Cycle of Hurricane Gilbert. *Monthly Weather Review*, *120*(6), 947–957. https://doi.org/10.1175/1520-0493(1992)120<0947:TCECOH>2.0.CO;2

Chavas, D. R., Lin, N., & Emanuel, K. (2015). A Model for the Complete Radial Structure of the Tropical Cyclone Wind Field. Part I: Comparison with Observed Structure*. *Journal of the Atmospheric Sciences*, *72*(9), 3647–3662. https://doi.org/10.1175/JAS-D-15-0014.1

Cheng, C.-J., & Wu, C.-C. (2018). The Role of WISHE in Secondary Eyewall Formation. *Journal of the Atmospheric Sciences*, *75*(11), 3823–3841. https://doi.org/10.1175/JAS-D-17-0236.1

Dai, Y., Majumdar, S. J., & Nolan, D. S. (2017). Secondary Eyewall Formation in Tropical Cyclones by Outflow–Jet Interaction. *Journal of the Atmospheric Sciences*, *74*(6), 1941–1958. https://doi.org/10.1175/JAS-D-16-0322.1

Emanuel, K. (2004). Tropical cyclone energetics and structure. In E. Fedorovich, R. Rotunno, & B. Stevens (Eds.), *Atmospheric Turbulence and Mesoscale Meteorology* (1st ed., pp. 165–192). Cambridge University Press. https://doi.org/10.1017/CBO9780511735035.010

Emanuel, K. (2017). Assessing the present and future probability of Hurricane Harvey's rainfall. *Proceedings of the National Academy of Sciences*, *114*(48), 12681–12684. https://doi.org/10.1073/pnas.1716222114

Emanuel, K., & Rotunno, R. (2011). Self-Stratification of Tropical Cyclone Outflow. Part I: Implications for Storm Structure. *Journal of the Atmospheric Sciences*, *68*(10), 2236–2249. https://doi.org/10.1175/JAS-D-10-05024.1

Fang, J., & Zhang, F. (2012). Effect of Beta Shear on Simulated Tropical Cyclones. *Monthly Weather Review*, *140*(10), 3327–3346. https://doi.org/10.1175/MWR-D-10-05021.1

Feldmann, M., Emanuel, K., Zhu, L., & Lohmann, U. (2019). Estimation of Atlantic Tropical Cyclone Rainfall Frequency in the United States. *Journal of Applied Meteorology and Climatology*, *58*(8), 1853–1866. https://doi.org/10.1175/JAMC-D-19-0011.1

Ge, X. (2015). Impacts of environmental humidity on concentric eyewall structure: The impact of moisture on TC structure. *Atmospheric Science Letters*, *16*(3), 273–278. https://doi.org/10.1002/asl2.553

Gori, A., Lin, N., Xi, D., & Emanuel, K. (2022). Tropical cyclone climatology change greatly exacerbates US extreme rainfall–surge hazard. *Nature Climate Change*, *12*(2), 171–178. https://doi.org/10.1038/s41558-021-01272-7

Hawkins, J. D., & Helveston, M. (2004). Tropical cyclone multiple eyewall characteristics (pp. 276–277). Presented at the Preprints AMS 26th Hurricane and Tropical Meteorology Conference.

Hawkins, J. D., Helveston, M., Lee, T. F., Turk, F. J., Richardson, K., Sampson, C., et al. (2006). Tropical Cyclone Multiple Eyewall Configurations. Presented at the Preprints AMS 27th Hurricane and Tropical Meteorology Conference.

Hence, D. A., & Houze, R. A. (2012). Vertical Structure of Tropical Cyclones with Concentric Eyewalls as Seen by the TRMM Precipitation Radar. *Journal of the Atmospheric Sciences*, *69*(3), 1021–1036. https://doi.org/10.1175/JAS-D-11-0119.1

Hill, K. A., & Lackmann, G. M. (2009). Influence of Environmental Humidity on Tropical Cyclone Size. *Monthly Weather Review*, *137*(10), 3294–3315. https://doi.org/10.1175/2009MWR2679.1

Holland, G. J. (1980). An Analytic Model of the Wind and Pressure Profiles in Hurricanes. *Monthly Weather Review*, *108*(8), 1212–1218. https://doi.org/10.1175/1520-0493(1980)108<1212:AAMOTW>2.0.CO;2

Holland, G. J. (2010). A Revised Model for Radial Profiles of Hurricane Winds. *Monthly Weather Review*, *138*(12), 4393–4401. https://doi.org/10.1175/2010MWR3317.1

Houze, R. A., Chen, S. S., Smull, B. F., Lee, W.-C., & Bell, M. M. (2007). Hurricane Intensity and Eyewall Replacement. *Science*, *315*(5816), 1235–1239. https://doi.org/10.1126/science.1135650

Huang, Y.-H., Montgomery, M. T., & Wu, C.-C. (2012). Concentric Eyewall Formation in Typhoon Sinlaku (2008). Part II: Axisymmetric Dynamical Processes. *Journal of the Atmospheric Sciences*, *69*(2), 662–674. https://doi.org/10.1175/JAS-D-11-0114.1

Judt, F., & Chen, S. S. (2010). Convectively Generated Potential Vorticity in Rainbands and Formation of the Secondary Eyewall in Hurricane Rita of 2005. *Journal of the Atmospheric Sciences*, *67*(11), 3581–3599. https://doi.org/10.1175/2010JAS3471.1

Kepert, J. D. (2013). How Does the Boundary Layer Contribute to Eyewall Replacement Cycles in Axisymmetric Tropical Cyclones? *Journal of the Atmospheric Sciences*, *70*(9), 2808–2830. https://doi.org/10.1175/JAS-D-13-046.1

Knapp, K. R., Kruk, M. C., Levinson, D. H., Diamond, H. J., & Neumann, C. J. (2010). The International Best Track Archive for Climate Stewardship (IBTrACS): Unifying Tropical Cyclone Data. *Bulletin of the American Meteorological Society*, *91*(3), 363–376. https://doi.org/10.1175/2009BAMS2755.1

Knapp, K. R., Diamond, H. J., Kossin, J. P., Kruk, M. C., & Schreck, C. J. (2018). International Best Track Archive for Climate Stewardship (IBTrACS) Project, Version 4 [Data set]. NOAA National Centers for Environmental Information. https://doi.org/10.25921/82TY-9E16

Kossin, J. P. (2015). Hurricane Wind–Pressure Relationship and Eyewall Replacement Cycles. *Weather and Forecasting*, *30*(1), 177–181. https://doi.org/10.1175/WAF-D-14-00121.1

Kossin, J. P., & DeMaria, M. (2016). Reducing Operational Hurricane Intensity Forecast Errors during Eyewall Replacement Cycles. *Weather and Forecasting*, *31*(2), 601–608. https://doi.org/10.1175/WAF-D-15-0123.1

Kossin, J. P., & Sitkowski, M. (2009a). An Objective Model for Identifying Secondary Eyewall Formation in Hurricanes. *Monthly Weather Review*, *137*(3), 876–892. https://doi.org/10.1175/2008MWR2701.1

Kossin, J. P., & Sitkowski, M. (2009b). An Objective Model for Identifying Secondary Eyewall Formation in Hurricanes. *Monthly Weather Review*, *137*(3), 876–892. https://doi.org/10.1175/2008MWR2701.1

Kuo, H-C., Lin, L.-Y., Chang, C.-P., & Williams, R. T. (2004). The Formation of Concentric Vorticity Structures in Typhoons. *Journal of the Atmospheric Sciences*, *61*(22), 2722–2734. https://doi.org/10.1175/JAS3286.1

Kuo, Hung-Chi, Schubert, W. H., Tsai, C.-L., & Kuo, Y.-F. (2008). Vortex Interactions and Barotropic Aspects of Concentric Eyewall Formation. *Monthly Weather Review*, *136*(12), 5183–5198. https://doi.org/10.1175/2008MWR2378.1

Kuo, Hung-Chi, Chang, C.-P., Yang, Y.-T., & Jiang, H.-J. (2009). Western North Pacific Typhoons with Concentric Eyewalls. *Monthly Weather Review*, *137*(11), 3758–3770. https://doi.org/10.1175/2009MWR2850.1

Lu, P., Lin, N., Emanuel, K., Chavas, D., & Smith, J. (2018). Assessing Hurricane Rainfall Mechanisms Using a Physics-Based Model: Hurricanes Isabel (2003) and Irene (2011). *Journal of the Atmospheric Sciences*, *75*(7), 2337–2358. https://doi.org/10.1175/JAS-D-17-0264.1

Lu, P., Done, J. M., Jing, R., Yang, L., Li, Y., Wang, D., & Lin, Y. (2022). *A Simple Diagnostic for Assessing Internal Dynamical Constraints on Tropical Cyclone Intensity* (preprint). https://doi.org/10.21203/rs.3.rs-2060046/v1

May, P. T., & Holland, G. J. (1999). The Role of Potential Vorticity Generation in Tropical Cyclone Rainbands. *Journal of the Atmospheric Sciences, 56*(9), 1224–1228. https://doi.org/10.1175/1520-0469(1999)056<1224:TROPVG>2.0.CO;2

Molinari, J., & Vollaro, D. (1990). External Influences on Hurricane Intensity. Part II: Vertical Structure and Response of the Hurricane Vortex. *Journal of the Atmospheric Sciences*, *47*(15), 1902–1918. https://doi.org/10.1175/1520-0469(1990)047<1902:EIOHIP>2.0.CO;2

Montgomery, M. T., & Kallenbach, R. J. (1997). A theory for vortex rossby-waves and its application to spiral bands and intensity changes in hurricanes. *Quarterly Journal of the Royal Meteorological Society*, *123*(538), 435–465. https://doi.org/10.1002/qj.49712353810

Nong, S., & Emanuel, K. (2003). A numerical study of the genesis of concentric eyewalls in hurricanes. *Quarterly Journal of the Royal Meteorological Society*, *129*(595), 3323–3338. https://doi.org/10.1256/qj.01.132

Ooyama, K. (1969). Numerical Simulation of the Life Cycle of Tropical Cyclones. *Journal of the Atmospheric Sciences*, *26*(1), 3–40. https://doi.org/10.1175/1520-0469(1969)026<0003:NSOTLC>2.0.CO;2

Rozoff, C. M., Schubert, W. H., McNoldy, B. D., & Kossin, J. P. (2006). Rapid Filamentation Zones in Intense Tropical Cyclones. *Journal of the Atmospheric Sciences*, *63*(1), 325–340. https://doi.org/10.1175/JAS3595.1

Rozoff, C. M., Nolan, D. S., Kossin, J. P., Zhang, F., & Fang, J. (2012). The Roles of an Expanding Wind Field and Inertial Stability in Tropical Cyclone Secondary Eyewall Formation. *Journal of the Atmospheric Sciences*, *69*(9), 2621–2643. https://doi.org/10.1175/JAS-D-11-0326.1

Sitkowski, M., Kossin, J. P., & Rozoff, C. M. (2011). Intensity and Structure Changes during Hurricane Eyewall Replacement Cycles. *Monthly Weather Review*, *139*(12), 3829–3847. https://doi.org/10.1175/MWR-D-11-00034.1

Terwey, W. D., & Montgomery, M. T. (2008). Secondary eyewall formation in two idealized, full-physics modeled hurricanes. *Journal of Geophysical Research*, *113*(D12), D12112. https://doi.org/10.1029/2007JD008897

TMI. (2017). GPM TMI on TRMM Brightness Temperatures L1B 1.5 hours 13 km V05 [Data set]. NASA Goddard Earth Sciences Data and Information Services Center. https://doi.org/10.5067/GPM/TMI/TRMM/1B/05

Wang, Y. (2009). How Do Outer Spiral Rainbands Affect Tropical Cyclone Structure and Intensity?*. *Journal of the Atmospheric Sciences*, *66*(5), 1250–1273. https://doi.org/10.1175/2008JAS2737.1

Wentz, F. J., Mears, C. A., & NOAA CDR Program. (2013). NOAA Climate Data Record (CDR) of SSM/I and SSMIS Microwave Brightness Temperatures, RSS Version 7 [Data set]. NOAA National Centers for Environmental Information. https://doi.org/10.7289/V5SJ1HKZ

Willoughby, H. E., Clos, J. A., & Shoreibah, M. G. (1982). Concentric Eye Walls, Secondary Wind Maxima, and The Evolution of the Hurricane vortex. *Journal of the Atmospheric Sciences*, *39*(2), 395–411. https://doi.org/10.1175/1520-0469(1982)039<0395:CEWSWM>2.0.CO;2

Xi, D., Lin, N., & Smith, J. (2020). Evaluation of a Physics-Based Tropical Cyclone Rainfall Model for Risk Assessment. *Journal of Hydrometeorology*, *21*(9), 2197–2218. https://doi.org/10.1175/JHM-D-20-0035.1

Yang, Y.-T., Kuo, H.-C., Hendricks, E. A., & Peng, M. S. (2013). Structural and Intensity Changes of Concentric Eyewall Typhoons in the Western North Pacific Basin. *Monthly Weather Review*, *141*(8), 2632–2648. https://doi.org/10.1175/MWR-D-12-00251.1

Zhou, X., & Wang, B. (2011). Mechanism of Concentric Eyewall Replacement Cycles and Associated Intensity Change. *Journal of the Atmospheric Sciences*, *68*(5), 972–988. https://doi.org/10.1175/2011JAS3575.1

Zhu, L., Quiring, S. M., & Emanuel, K. A. (2013). Estimating tropical cyclone precipitation risk in Texas: TROPICAL CYCLONE PRECIPITATION RISK. *Geophysical Research Letters*, *40*(23), 6225–6230. https://doi.org/10.1002/2013GL058284

Zhu, L., Emanuel, K., & Quiring, S. M. (2021). Elevated risk of tropical cyclone precipitation and pluvial flood in Houston under global warming. *Environmental Research Letters*, *16*(9), 094030. https://doi.org/10.1088/1748-9326/ac1e3d

Zhu, X.-S., & Yu, H. (2019). Environmental Influences on the Intensity and Configuration of Tropical Cyclone Concentric Eyewalls in the Western North Pacific. *Journal of the Meteorological Society of Japan. Ser. II*, *97*(1), 153–173. https://doi.org/10.2151/jmsj.2019-008

Figure1.

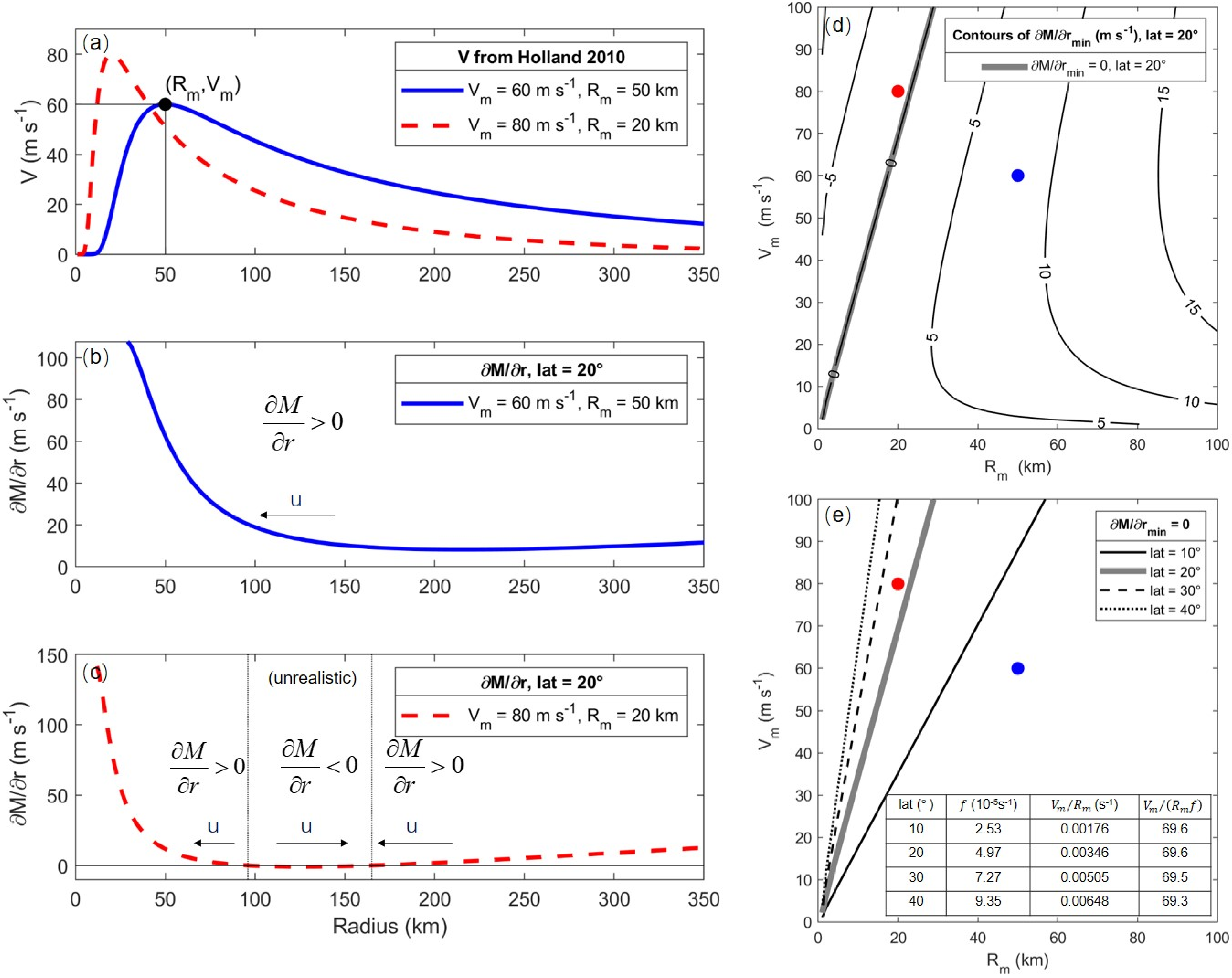
(a)
V from Holland 2010
V_m = 60 m s^{-1}, R_m = 50 km
V_m = 80 m s^{-1}, R_m = 20 km
(R_m, V_m)
V (m s^{-1})
(b)
∂M/∂r, lat = 20°
V_m = 60 m s^{-1}, R_m = 50 km
$\frac{\partial M}{\partial r} > 0$
u
∂M/∂r (m s^{-1})
(c)
(unrealistic)
∂M/∂r, lat = 20°
V_m = 80 m s^{-1}, R_m = 20 km
$\frac{\partial M}{\partial r} > 0$
$\frac{\partial M}{\partial r} < 0$
$\frac{\partial M}{\partial r} > 0$
u
u
u
∂M/∂r (m s^{-1})
Radius (km)
(d)
Contours of $\partial M/\partial r_{min}$ (m s^{-1}), lat = 20°
$\partial M/\partial r_{min}$ = 0, lat = 20°
V_m (m s^{-1})
R_m (km)
(e)
$\partial M/\partial r_{min}$ = 0
lat = 10°
lat = 20°
lat = 30°
lat = 40°
V_m (m s^{-1})
R_m (km)
lat (°) | f (10^{-5}s^{-1}) | V_m/R_m (s^{-1}) | $V_m/(R_m f)$
10 | 2.53 | 0.00176 | 69.6
20 | 4.97 | 0.00346 | 69.6
30 | 7.27 | 0.00505 | 69.5
40 | 9.35 | 0.00648 | 69.3

Figure2.

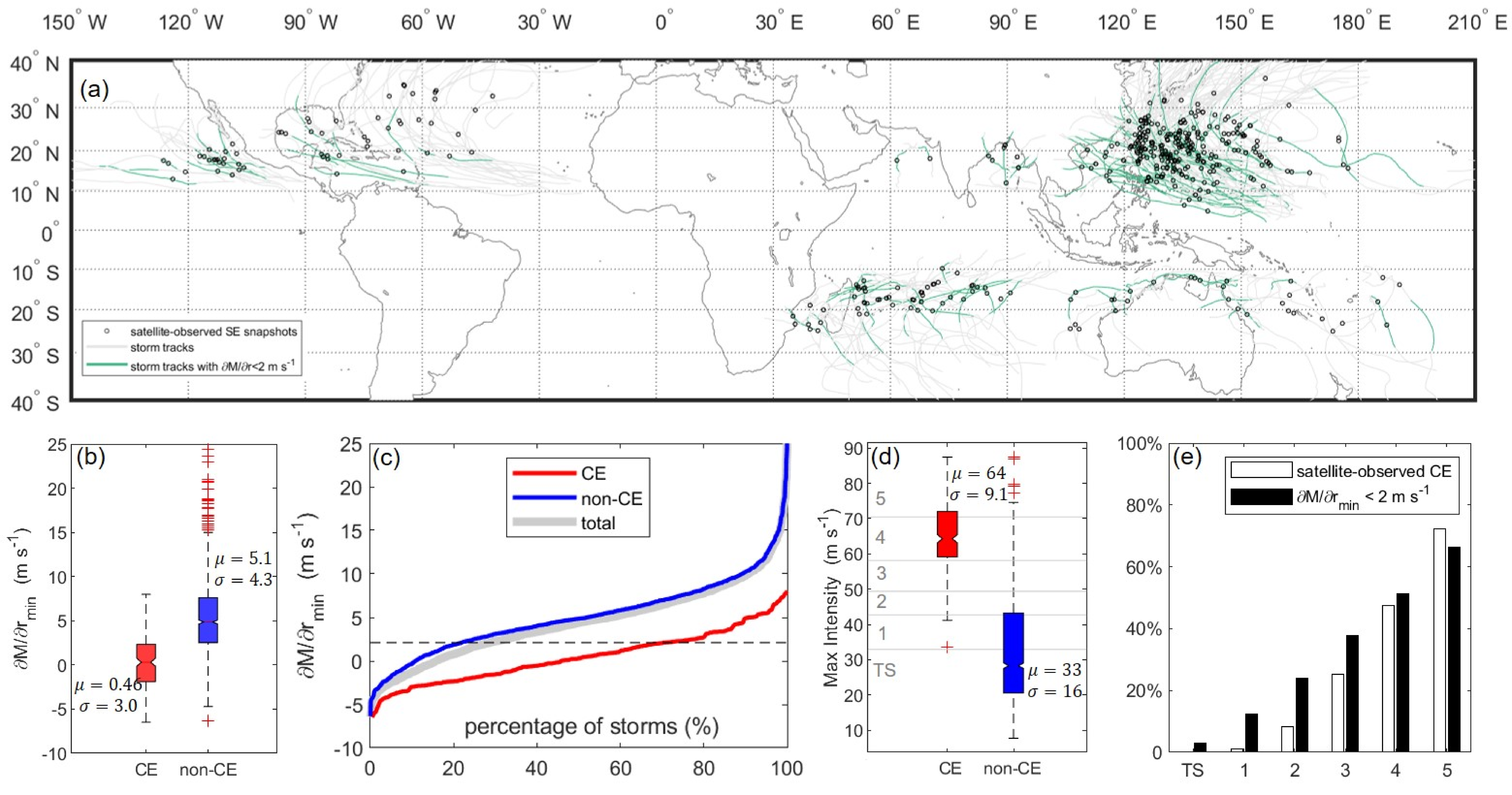

(a)
satellite-observed SE snapshots
storm tracks
storm tracks with ∂M/∂r<2 m s-1
150° W 120° W 90° W 60° W 30° W 0° 30° E 60° E 90° E 120° E 150° E 180° E 210° E
40° N 30° N 20° N 10° N 0° 10° S 20° S 30° S 40° S
(b)
∂M/∂r min (m s-1)
μ = 0.46
σ = 3.0
μ = 5.1
σ = 4.3
CE non-CE
(c)
CE
non-CE
total
percentage of storms (%)
(d)
Max Intensity (m s-1)
μ = 64
σ = 9.1
μ = 33
σ = 16
5 4 3 2 1 TS
CE non-CE
(e)
satellite-observed CE
∂M/∂r min < 2 m s-1
TS 1 2 3 4 5

Figure3.

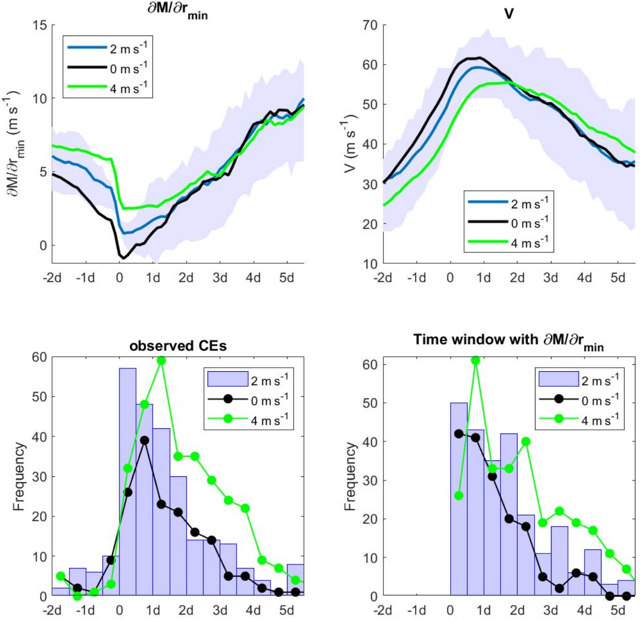

∂M/∂r_min
15
10
5
0
∂M/∂r_min (m s^-1)
2 m s^-1
0 m s^-1
4 m s^-1
-2d
-1d
0
1d
2d
3d
4d
5d
V
70
60
50
40
30
20
10
V (m s^-1)
observed CEs
Frequency
Time window with ∂M/∂r_min

Figure4.

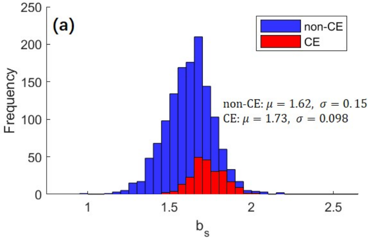

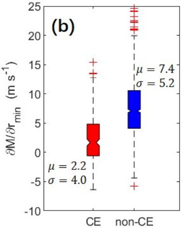

(c)	$V_m/(R_m f)$ on $\dfrac{\partial M}{\partial r}_{min} = 0$ with varying b_s and latitudes					
lat (°)	$b_s = 1.4$	$b_s = 1.5$	$b_s = 1.6$	$b_s = 1.7$	$b_s = 1.8$	$b_s = 1.9$
10	114.4	102.5	91.1	80.1	69.6	59.6
20	114.3	102.4	91.0	80.1	69.6	59.6
30	114.2	102.3	91.0	80.0	69.5	59.5
40	114.1	102.2	90.8	79.9	69.3	59.4